Resolved imaging of the HD 191089 debris disc

Laura Churcher,[1][*] Mark Wyatt[1] and Rachel Smith[2]

[1]*Institue of Astronomy, University of Cambridge, Madingley Road, Cambridge CB3 0HA*
[2]*Astrophysics Group, Keele University, Staffordshire ST5 5BG*

ABSTRACT

Two-thirds of the F star members of the 12 Myr old β Pictoris moving group (BPMG) show significant excess emission in the mid-infrared, several million years after the expected dispersal of the protoplanetary disc. Theoretical models of planet formation suggest that this peak in the mid-infrared emission could be due to the formation of Pluto-sized bodies in the disc, which ignite the collisional cascade and enhance the production of small dust. Here we present resolved mid-infrared imaging of the disc of HD 191089 (F5V in the BPMG) and consider its implications for the state of planet formation in this system. HD 191089 was observed at 18.3 µm using T-ReCS on Gemini South and the images were compared to models of the disc to constrain the radial distribution of the dust. The emission observed at 18.3 µm is shown to be significantly extended beyond the point spread function (PSF) at a position angle of 80°. This is the first time dust emission has been resolved around HD 191089. Modelling indicates that the emission arises from a dust belt from 28 to 90 au, inclined at 35° from edge on with very little emission from the inner 28 au of the disc, indicating the presence of an inner cavity. The steep slope of the inner edge is more consistent with truncation by a planet than with ongoing stirring. A tentative brightness asymmetry $F_W/F_E = 0.80 \pm 0.12 \, (1.8\sigma)$ between the two sides of the disc could be evidence for perturbations from a massive body on an eccentric orbit in the system.

Key words: planets and satellites: formation – circumstellar matter – stars: individual: H191089.

1 INTRODUCTION

The majority ($\geq$80 per cent) of stars are born with protoplanetary discs (Haisch, Lada & Lada 2001) which are massive and contain large amounts of gas, with an estimated gas to dust ratio of 100:1 (Andrews & Williams 2005). These discs have a lifetime of ∼6 Myr (Haisch et al. 2001) and at ages of a few Myr undergo a transition, the nature of which is still unclear (Muzerolle et al. 2010). Some protoplanetary discs have inner holes (Luhman et al. 2010) but the systems retain an optically thick outer disc and are often called transition discs to signify that this is a phase that discs go through. At later times (∼10 Myr) the remaining optically thick material in the disc has also disappeared, leaving optically thin debris discs.

Debris discs surround ∼15 per cent of main-sequence stars (see Wyatt 2008 for a recent review). The dust particles in debris discs are generally small, and so are subject to radiation forces such as radiation pressure and Poynting–Robertson (P-R) drag from the central star (Backman & Paresce 1993) which remove grains from the system on time-scales much shorter than the stellar lifetime so the dust must be continuously replenished. The collisional destruc-

tion or sublimation of larger bodies (planetesimals) can create such dust particles. Effectively, the small dust can be used as a tracer for the presence of bodies many hundreds of kilometres in size that are otherwise undetectable. Inner cavities have also been observed in debris discs, either directly through images or indirectly through an absence of hot dust. The holes imply a lack of planetesimals in the inner region, as rapid collisional processing means that none of the dust created in the outer disc reaches the inner region (Wyatt 2006).

Since gas giants must form in the gas-rich protoplanetary disc then it is possible that the planetary system is fully formed by the end of the transition phase. Imaging of debris discs at ages of ∼10 Myr shows evidence that planet formation in these systems has already finished and formed Jupiter mass planets. The existence of such planets was inferred from debris disc observations (Wyatt et al. 2005; Quillen 2006) and subsequently confirmed through direct imaging of planets in systems such as the ∼8 M_{jup} planet imaged around β Pic, a 10 Myr old A star with a debris disc (Lagrange et al. 2009) and a <3 M_{jup} planet imaged around Fomalhaut (Kalas et al. 2008; Chiang et al. 2009).

However models indicate that the growth of solid objects in a debris disc can continue for several 100 Myr (Kenyon & Bromley 2004). In such self-stirred models a bright ring appears in an extended planetesimal disc where Pluto-sized bodies have just formed.

[*]E-mail: ljc51@ast.cam.ac.uk

These bodies stir the planetesimal belt into collisional destruction and increase dust production, causing the disc to brighten at this location. There is some evidence in favour of this; observations of a peak in the brightness of debris discs around A stars at ages of 5 to 10 Myr (Currie et al. 2008) can be explained in this context but a more detailed examination indicates that these models still require an inner hole to reproduce the observations. The inner region could have been cleared by a planet that is then stirring the outer regions of the disc (Kennedy & Wyatt 2010).

Resolved imaging of young debris discs is therefore important in discriminating between discs being perturbed by a fully formed planet, such as in the pericentre glow model applied to HR 4796 (Wyatt et al. 1999) and discs in which planet formation may still be ongoing such as η Tel (Smith et al. 2009) where the disc is modelled using the delayed stirring models of Kenyon & Bromley (2004).

Many young stars are too distant to study their discs in detail, but young moving groups in this age range such as the β Pictoris moving group (BPMG) (12 Myr) provide a relatively nearby, young population in which to assess the origin and diversity of debris disc emission at this age (Zuckerman & Song 2004).

HD 191089 (HIP 99273) is an F5V star at a distance of 54 pc (Perryman, Lindegren & Kovalevsky 1997) that was identified as a candidate debris disc by Mannings & Barlow (1998) based on *IRAS* photometry. The age of this source is somewhat uncertain and estimates in the literature vary widely. Isochrone fitting suggests older ages, with Nordström et al. (2004) giving an age of 3 Gyr and Chen et al. (2006) finding 1.6 Gyr. However, when considering evidence of youth such as X-Ray emission and lithium abundance data amongst other techniques, the age indicated is significantly younger; Zuckerman & Song (2004) find 100 Myr. However, Moór et al. (2006) suggest that the source is a possible member of the BPMG due to HD 191089's proper motion and high rotation rate, giving it an age of 12 Myr. This membership appears to be confirmed from further proper motion studies by Lépine & Simon (2009). The BPMG is a rich source of debris discs with ∼23 per cent (Rebull et al. 2008) of members harbouring a disc. Here, we adopt an age of 12 Myr when interpreting this source.

Using the *Spitzer* fluxes for this source (Hillenbrand et al. 2008) and other Sun-like stars, an analysis similar to that presented in Smith & Wyatt (2010) for A star debris discs showed that HD 191089 was the most favourable target for imaging debris discs with deep mid-IR observations.

In Section 2 we present 18.3 μm imaging of HD 191089 taken with the T-ReCS instrument on Gemini South. In Section 3 we analyse these observations and show that we have resolved the debris disc. In Section 4 we confront these observations with models to determine the disc parameters, and in Section 5 discuss the implications of the inferred structure for the status of planet formation in this system, both in the context of the pericentre glow model (Wyatt et al. 1999) and the self-stirred model (Kenyon & Bromley 2004).

2 OBSERVATIONS

These observations were taken under proposal GS-2009A-28 using T-ReCS on Gemini South with filter Qa ($\lambda_c = 18.3$ μm, $\Delta\lambda = 1.51$ μm). The pixel scale of the T-ReCS instrument is 0.09 arcsec and the total field of view of is 29×22 arcsec^2. These observations were taken in parallel chop-nod mode with a chop throw of 15 arcsec and chop position angle (PA) of 55° (east of north). The data were taken over three nights (2009 June 9, 2009 July 12 and 2009 July 13). The total on source time was 7200 s. Observations of standard star HD 189831 (spectral type K5III) listed in Cohen et al. (1999) were made to calibrate the photometry and also to monitor the point spread function (PSF) of the observations. The order of the observations and the on source integration times are shown in Table 1.

These data for HD 191089 were taken in sets of four 360 s long integrations with six complete nod cycles (ABBA). The data were reduced using custom routines described in Smith, Wyatt & Dent (2008). The data reduction involved determining a gain map for each observation using the mean values of each frame to construct a map of pixel responsivity. The on-source pixels were masked during this process, making this equivalent to a sky flat-field frame. A DC offset was then determined by calculating the mean pixel values in every row and every column, again masking pixels where there was source emission present. This was then subtracted from the final image to ensure a flat background. Pixels which showed high or low gain in comparison with the median response throughout the observation were masked off. In order to avoid errors in co-adding the data which could arise from misalignment of the images, we

Table 1. Observations taken under proposal GS-2009A-Q-28 in order. Note that the on source time is half of the total integration time listed in the table. Fluxes are for a 1 arcsec radius aperture centred on the star. The group indicates the standard-science-standard observing pattern used. One standard was used in groups 2 and 3 due to an omitted calibration observation. Each science observation consists of four subintegrations.

Date (dd/mm/yy)	Object	Group	Name	Filter	Integration time (s)	Calibrated flux (mJy)
09/06/09	HD 189831	1	Std1	*QA*	120	3441
09/06/09	HD 191089	1	Im1	*QA*	1440	158 ± 21
09/06/09	HD 189831	1	Std2	*QA*	120	3441
12/07/09	HD 189831	2	Std3	*QA*	1440	3441
12/07/09	HD 191089	2	Im2	*QA*	1440	167 ± 22
12/07/09	HD 189831	2/3	Std4	*QA*	120	3441
12/07/09	HD 191089	3	Im3	*QA*	1440	166 ± 23
12/07/09	HD 189831	3	Std5	*QA*	120	3441
12/07/09	HD 189831	4	Std6	*QA*	120	3441
12/07/09	HD 191089	4	Im4	*QA*	1440	145 ± 24
12/07/09	HD 189831	4	Std7	*QA*	120	3441
13/07/09	HD 189831	5	Std8	*QA*	120	3441
13/07/09	HD 191890	5	Im5	*QA*	1440	174 ± 31
13/07/09	HD 189831	5	Std9	*QA*	120	3441

fitted a Gaussian with a subpixel centroid to accurately determine the centre of the image and so the position of the star. The rebinning was done using bilinear interpolation across the array.

The standard star was observed at a similar airmass to HD 191089. The calibration levels were compared with the airmass for the standard star observations and no correlation was found, so no extinction correction was applied to the calibration factors.

In order to calibrate the images an average of the calibration factors determined from standard star observations was used. The standard star, HD 189831 ($F_{18} = 3.44$ Jy from Cohen et al. 1999; Adelman 2001) was observed twice per group of observations (see Table 1 for detail of observations groups). A co-add of the two standards from each group was used to calibrate the observations of HD 191089 in the same group. The average calibration error for the five groups of observations was 6 per cent. The groups had calibration factors that varied by 3, 6, 12, 6 and 4 per cent. These values were used to calculate a calibration error for the fluxes. These centred, flux-calibrated images from each group were then used to produce final images of HD 191089 and the standard star.

3 RESULTS

The final co-added images for HD 191089 and the standard star HD 189831 for PSF reference are shown in Fig. 1. The solid line contours shown in the images are 25, 50 and 75 per cent of the peak for both HD 191089 and the standard. The dashed contour represents 10 per cent of the peak emission. The peak value for HD 191089 in the final co-added Qa image is 344 mJy arcsec^{-2} and the peak value for the standard is 27 648 mJy arcsec^{-2}.

Photometry was performed using a 1.0 arcsec radius circular aperture centred on the star. The stellar flux in the Qa filter is expected to be 44 mJy from the K-band flux (see Section 4.2). Our photometry yields a flux of 163 ± 22 mJy including both calibration and photometric errors for the final co-added image of HD 191089 shown in Fig. 1 with a signal-to-noise ratio (S/N) of 38 (not including calibration errors). Thus the photometry gives an excess of 119 ± 22 mJy in a 1 arcsec radius aperture centred on the star. The IRS

spectrum of Chen et al. (2006) after subtraction of the stellar flux gives an excess of 115 ± 3 mJy. The T-ReCs photometry presented here therefore agrees with the IRS results. It does not appear that the IRS spectrum includes any emission centred on the star outside the 1-arcsec aperture used here for photometry, as might happen in the larger IRS beam (extracted along a 3.7-arcsec slit). The total error on the photometric measurements in Table 1 consists of both the calibration error and the statistical noise. The statistical noise was determined using an annulus with an inner radius of 3 arcsec and an outer radius of 4 arcsec centred on the star, resulting in an error averaged over all the groups of 1.1 mJy arcsec^{-2}.

There is clear ellipticity in the image of HD 191089 (centre of Fig. 1) and a 2D Gaussian fit to HD 191089 gives the ellipticity of the image at the 50 per cent contour as 0.104 ± 0.015 with the major axis at PA $80° \pm 10°$ east of north. The same ellipticity is seen on all three nights. In comparison the ellipticity of the standard was 0.024 ± 0.007 with the major axis at a PA $55° \pm 2°$ east of north. As all the observations were performed with no on-sky rotation and chop-nod performed at $55°$ east of north, the ellipticity in the PSF could be due to chop smearing, but the extension seen in the HD 19089 images is at a very different PA and so is unlikely to be an artefact of the chopping process.

The right-hand image in Fig. 1 is the residual image of HD 191089 after the subtraction of the standard star image scaled to the flux expected from the photosphere of HD 191089 (44 mJy) followed by smoothing by a Gaussian of width 4 pixels. Scaling the subtraction to the expected stellar flux means that we are not removing any of the disc emission. We also tried subtracting the standard star image scaled to the peak of the HD 191089 image, to see if there was any additional unresolved flux present at the peak, and found that this results in a subtraction of 49 mJy, indicating that there is very little unresolved disc flux contributing to the peak. A ring is seen in the residual image, consistent with a disc that is at some intermediate inclination between edge on and face on. The PA of the peaks (and hence the major axis of the ring) was found by finding the angle between the peaks in the residual image and was found to be at $80° \pm 10°$ east of north, consistent with the orientation of the
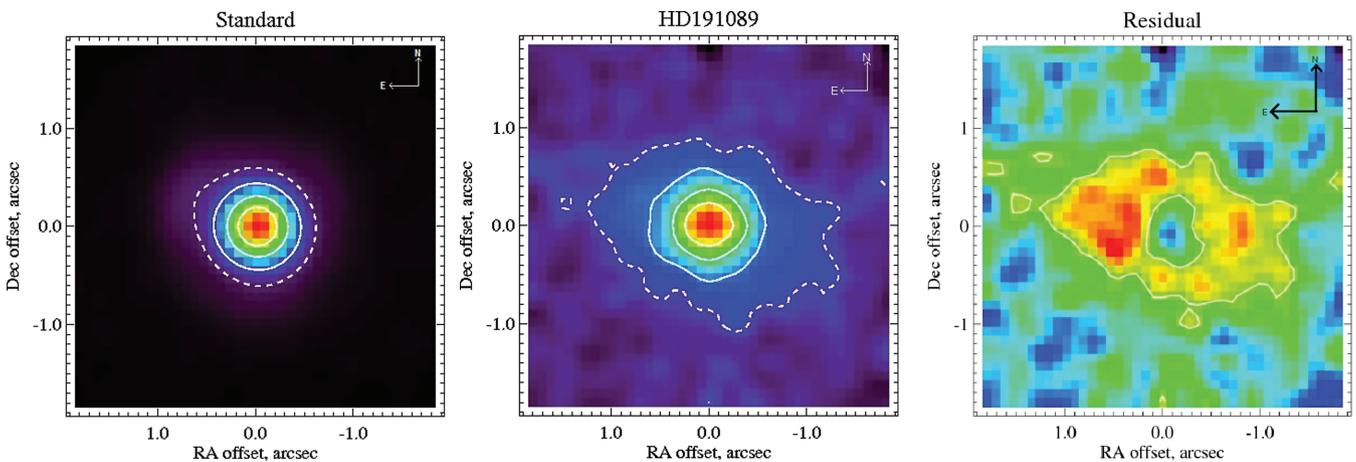

Figure 1. Left to right: the final co-added images of the standard star (left) and HD 191089 (centre) and a residual emission image shown after subtracting an azimuthally symmetric PSF created from the standard star image scaled to the expected photospheric emission from HD 191089 (44 mJy) from the science image (centre). Note that the distinct ellipticity seen in the image of HD 191089 is not seen in the standard star. Contours on the left and central plots are at 25, 50 and 75 per cent of the peak (solid lines) and 10 per cent of the peak (dashed line). The contours on the residual emission image are at 25, 50 and 75 per cent of the peak. Orientation of the images is north up, east left. The peak value for HD 191089 in QA is 344 mJy arcsec^{-2} and the peak value for the standard is 27 648 mJy arcsec^{-2}. The peak value for the residuals is 55 mJy arcsec^{-2}. The residual image has been smoothed by convolving with a Gaussian with a width of 4 pixels. The colour scale is linear from 0 to the maximum pixel value in each image.

ellipticity found for the science observations before subtraction of the PSF.

In order to assess the robustness of this putative disc, and to ensure that it is not an artefact of the PSF, we examined the temporal variability of the full width at half-maximum (FWHM) of the science data and assessed the significance of the extension. We also looked for any dependence of the FWHM on time or airmass. We took line-cuts at PA corresponding to the major and minor axes of the fitted ellipticity in the science images (PA 80° and 170°) for each group of HD 191089 observations (see Table 1 for observation groups) and for PSF standards from each observational group. The linecuts were smoothed by a Gaussian of width 3 pixels and were then fitted with a Gaussian profile to determine the FWHM. No dependence on airmass or time was found, and the median FWHM values and standard errors were found to be 8.81 ± 0.2 pixels at 80° for the standard, 9.95 ± 0.3 pixels at 80° for HD 191089, 8.10 ± 0.1 pixels at 170° for the standard and 9.46 ± 0.4 pixels for HD 191089 at 170°. There is naturally a large degree of scatter in the intensity profiles, due to variations in observing conditions, but HD 191089 shows extension when compared to the standard at 80° and there is also some evidence of extension along the minor axis of the image at 170°. This is shown graphically in Fig. 2 which shows the linecuts through each integration (of 2880 s, see Table 1) of HD 191089 (diamonds) and corresponding standard star integrations (plus signs). HD 191089 also has broader wings than the standard star image at 80°.

The residual image of HD 191089 shown in Fig. 1 also shows tentative evidence for a brightness asymmetry between the two sides of the disc. The ratio of the flux in a 0.5 arcsec radius aperture, centred on the E peak (found by fitting a Gaussian at subpixel resolution) and the flux in an identical aperture centred at the same radial location on the W side was $F_W/F_E = 0.80$. This aperture size was chosen to maximize the asymmetry observed. An azimuthally symmetric PSF was used for the subtraction shown in Fig. 1, so this apparent brightness difference is not simply due to non-axisymmetric features in the PSF. This was also checked by looking for any systematic azimuthal variations in the PSF, and by redoing the subtraction using each of the 10 standards to quantify the effect of PSF variability on the measured asymmetry. It was found that variability in the PSF FWHM and asymmetries change the flux ratio by ± 0.02, or $<0.2\sigma$ significance. The final stacked PSF image used had a FWHM of 8.82 pixels at 80° and 8.10 pixels at 170°.

The significance of this putative asymmetry was assessed using a Monte Carlo method. We created 10 000 axisymmetric disc models (see Section 4.1), convolved these models with the axisymmetric PSF and added Poissonian noise consistent with the observed levels in the images (~ 0.1 mJy pixel^{-1}). This does not account for the effects of any spatially correlated noise, such as coherent variation in the PSF over the course of the observations, but when we examined the PSF from each group of observations (see Table 1) we found no systematic asymmetries. This modelling provides a first guess at the chance of observing such an asymmetry simply due to uncertainty from Poissonian noise in the images. The average observed asymmetry between the two sides of the image in these noisy asymmetric models was 12 per cent. The brightness asymmetry observed is then significant at the 1.8σ level.

4 MODELLING

In this section we present a model that fits both the 18-μm image and the full spectral energy distribution (SED) simultaneously. The fit is achieved using an iterative process: the spatial distribution is
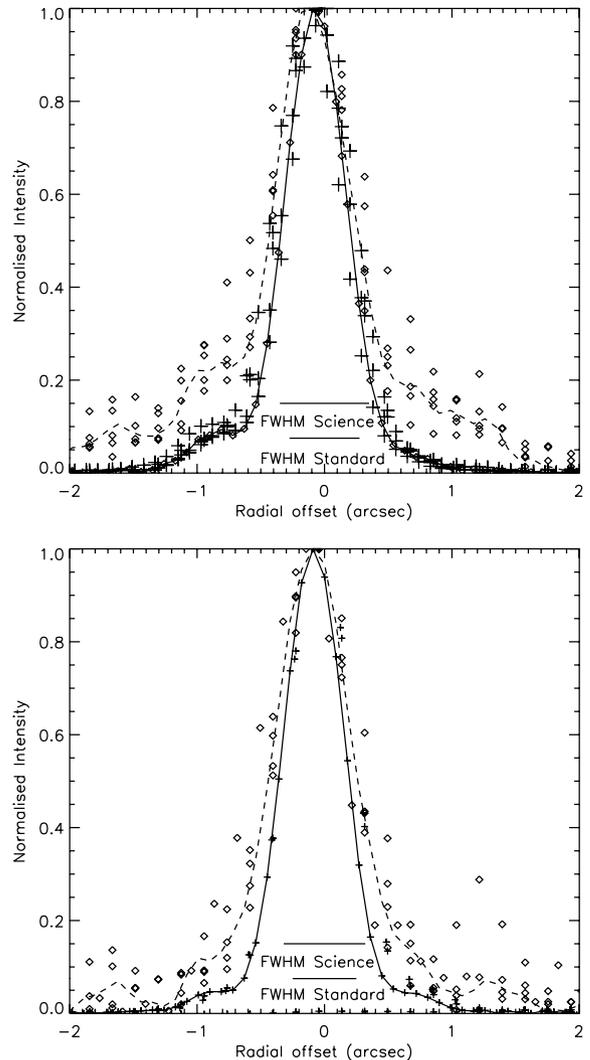

Figure 2. The profile of the line cuts through the total images at 80° east of north (top) and 170° east of north (bottom). The median FWHM measurements taken over all subintegrations from Gaussian fits to the profiles at the two angles are indicated for reference. The averaged profiles from all the line cuts for both HD 191089 and the standard star are also shown. The profile for HD 191089 (dashed line) at 80° is much broader in the wings than that of the standard star (solid line). There is also some evidence of a less pronounced extension at 170° as seen in the lower image. Note that multiple intensity profiles for the science target (diamonds) and the standard (crosses) are shown here. These are taken for each group as indicated in Table 1.

constrained from the image by assuming a nominal composition and size distribution (Section 4.1), then the dust model is constrained from the SED using the fitted spatial distribution (Section 4.2). This is possible because the SED fitting process fixes the total flux from the disc at 18 μm to be 115 mJy regardless of the assumed composition, and so this has little impact on the inferred spatial distribution. Further iterations of this process do not result in changes to either dust spatial distribution or composition.

4.1 Axisymmetric disc model

To determine constraints on the radial distribution of the emission seen in the resolved 18-μm image we first considered the simplest possible model of the disc structure. This model is composed of a

single axisymmetric disc component, defined by four free parameters: disc radius (r), width (dr), inclination (i) and surface density distribution Σ, which is assumed to have the form $\Sigma \propto r^\gamma$. The disc opening angle (which sets the disc height) is assumed to be $5°$ but this parameter is unconstrained by the modelling process. The flux from annuli in the disc at different radii was determined assuming a grain composition and size distribution that were constrained using the emission spectrum as outlined in Section 4.2.

In order to constrain the dust location, as well as the width of the disc, the inclination and the surface density profile, a grid of models was run. The model images were convolved with an azimuthally symmetric PSF and compared with the observed residuals using the images as well as the linecuts both in the direction of extension (PA $80°$) and perpendicular to the extension (PA $170°$). The use of both linecuts allowed us to constrain the inclination simultaneously with the radial morphology. The reduced chi-squared of the fit ($\chi_r^2 = [(obs - mod)^2/\nu] = 1$, where ν is the number of free parameters and 1 represents a good fit) to each of these three pieces of observational data were calculated and were then combined linearly with equal weight to come to a final mean reduced chi-squared [$\chi_{r_{combined}}^2 = (\chi_{rline_{80}}^2 + \chi_{rline_{170}}^2 + \chi_{rres}^2)/3$] which was then minimized across the grid of models. The ranges of model parameters tested were R_{in}: 10 to 50 au (1-au intervals), R_{out}: 50 to 100 au (5-au intervals), inclination: $10°$ to $60°$ ($5°$ intervals, where $0°$ is edge on), surface density index γ: -0.5 to -3.0 (0.5 intervals). The values for γ were chosen to cover possibilities such as the surface density distribution expected from grains being blown out of the system by radiation pressure ($\gamma = -1.0$), and that of the Minimum Mass Solar Nebular (MMSN) ($\gamma = -1.5$). The best-fitting model was found to be a ring at 28 ± 1 to 90 ± 5 au, with an inclination of $35° \pm 5°$ from edge on, and a surface density profile $\gamma = -1.5 \pm 0.5$. This best-fitting model had $\chi_{r_{combined}}^2 = 1.30$ with $\chi_{rline_{80}}^2 = 1.34$, $\chi_{rline_{170}}^2 = 1.40$, $\chi_{rres}^2 = 1.19$. The best-fitting model residual image is shown on the left of Fig. 3 and can be compared directly with the observed disc (Fig. 1, right) which has the same colour scale.
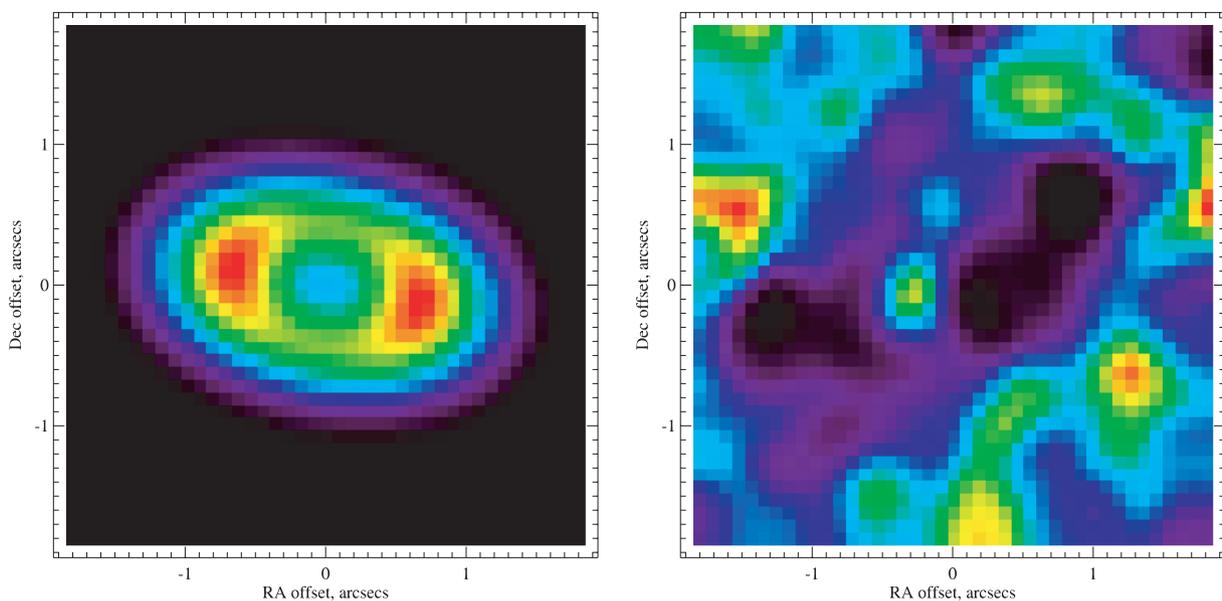
PSF variation can have an important impact on the observational residuals, and we used an azimuthally symmetric average PSF. This was motivated by the lack of effects of temporal and spatial variation in the PSF (see Section 3). The modelling process for the axisymmetric disc was repeated using the PSF with the largest FWHM (Std 8) and the smallest FWHM (Std 6) to find that PSF variation had no effect on the modelling results within the quoted errors.

4.2 SED models

The emission spectrum of HD 191089 is shown in Fig. 4. The stellar photospheric emission has been modelled using a Kurucz model atmosphere with a temperature of 6440 K (Kurucz 1979), fitted to the Two Micron All Sky Survey (2MASS) K-band photometry implying a stellar luminosity of $3.2\,L_\odot$ at the inferred distance of 53.5 pc. Photospheric flux contributions have been subtracted from the fluxes shown at $>5\,\mu m$ which thus represent the excess emission from the disc. This spectrum is approximately that of a blackbody fit with a temperature of 99 ± 9 K and a fractional luminosity ($f = L_{dust}/L_*$) of 1.5×10^{-3} (Chen et al. 2006).

The disc emission is calculated assuming the disc is optically thin. The emission from dust grains at a certain distance from the star is calculated using radiation balance with the stellar spectra as the input. The final spectra are then produced by integration over different radii and grain size. The grains were assumed to have a size distribution with $n(D) \propto D^{-3.5}$, where D is the grain diameter, which is the standard solution for a theoretical collisional cascade (see Dohnanyi 1969), that is truncated at a minimum and maximum grain size. For the assumed composition a grid of models was calculated with a range of minimum sizes 0.5–$10D_{bl}$, where D_{bl} is the largest grain size removed from the system by radiation pressure for which $\beta = 0.5$, where $\beta = F_{rad}/F_{grav}$, the ratio between radiation and gravitational forces (Burns, Lamy & Soter 1979) which depends on stellar properties, grain composition and porosity. The maximum size was fixed at 1 mm since larger grains have a negligible contribution to flux from a model with this size distribution.
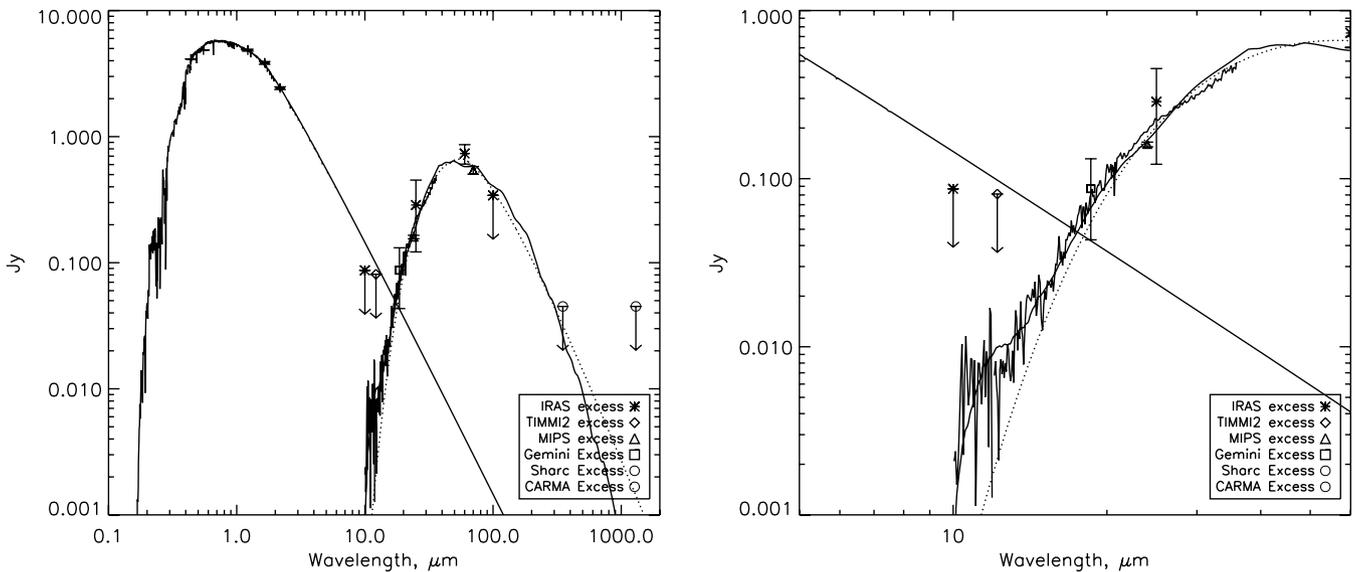

Figure 3. The best fitting axisymmetric disc model for the 18-μm emission (see Section 4.1). The model residual image (left) can be compared directly with the observed residuals (Fig. 1, right). The difference between the observed residuals and the model residuals (right) indicates an over subtraction near the disc ansae and a slight under subtraction at the peak. See section 5.1 for details.

Figure 4. SED of HD 191089. The photosphere of HD 191089 is fitted with a Kurucz model profile ($M_{star} = 1.4\,M_\odot, L_{star} = 3.2\,L_\odot, T_{star} = 6440$ K) scaled to the 2MASS K-band flux and shown with a solid line. Observations at $>5\,\mu$m are shown after the subtraction of the photospheric contributions: the IRS spectrum of Chen et al. 2006 (solid line from 5 to 30 μm), MIPS fluxes (Carpenter et al. 2009) (triangles) and IRAS colour-corrected excesses (asterisks) and Gemini TReCS fluxes in 0.5 arcsec radius aperture (square), and submm/mm upper limits (crosses) from SHARC and CARMA. The excess measurements are first fitted with a 99 K modified blackbody (dashed line), for comparison to a realistic grain fit (solid line) described in Section 4.2.

The grains were assumed to have a silicate core (amorphous olivine) and an accreted mantle of organic refractories produced by ultraviolet (UV) photoprocessing of ice (as used in Li & Greenberg 1997; Augereau et al. 1999). A range of compositions was also tried, with amorphous silicate fractions varying from 0 to 90 per cent by volume and with porosities (i.e. vacuum fraction of grain by volume) from 0 to 95 per cent. Dielectric constants were calculated from tabulated laboratory values (Li & Greenberg 1997; Augereau et al. 1999) using Maxwell–Garnett effective medium theory. The optical properties of the grains were calculated using Mie theory, Rayleigh–Gans theory and Geometric Optics in the appropriate size regimes (Bohren & Huffman 1983).

This resulted in a grid of 360 models over which χ^2 was minimized by fitting to the spectrum and MIPS fluxes (24 and 70 μm). The fit to the IRS spectrum was calculated using $\chi^2_{IRS} = (F_{obs} - F_{mod})^2/N$, where F_{obs} is the observed flux, F_{mod} is the model flux and N is the number of points in the observed IRS spectrum. This normalizes χ^2_{IRS} so that when calculating the final χ^2 the fit to the spectrum was given equal weight to the fits to the 24 and 70 μm MIPS fluxes. The best-fitting model with a reduced χ^2 of 1.14 has a minimum grain size that is coincident with the blow-out grain size (1.46 μm for the composition used) and a composition of amorphous silicate fraction of 10 per cent by volume, and a porosity of 60 per cent with the rest of the grain composed of organic refractory materials, with no ices present. The fractional luminosity is 1.4×10^{-3}. As there are no obvious spectral features in the SED, the main constraint on the composition and size distribution comes from allowing the appropriate range of temperatures to be present given the constraint that the dust is in the region 28–90 au; blackbody grains would have to be at a radius of 15 au to achieve the observed temperature. Although our model provides a consistent fit to both image and SED, it is not expected that the composition has been uniquely constrained by this process. This dust model was then used as an input to the model grid and there was no change to the best-fitting model of the 18-μm images.

The total mass in the collisional cascade, with the assumed size distribution of $n(D) \propto D^{-3.5}$ scales as $M_{tot} \propto \sqrt{D_{max}}$. Thus for $D_{max} = 1$ km the total mass would be 13 $M_\oplus$ two orders of magnitude higher than the current mass of the Kuiper belt (Bernstein et al. 2004), but note that we have no information on the maximum size of objects in this system.

4.3 Emptiness of the inner hole

It is possible to fit all excesses in the spectrum with a model that only extends from 28 to 90 au. There is no requirement either from the image or from the spectrum for emission at <28 au. The observed 18-μm image of HD 191089 shows a resolved belt of dust from 28 to 90 au, with a cleared inner region extending to a radius of ~28 au. We compared the photometry of the observations in the inner 28 au (0.5 arcsec radius aperture) and then repeated the measurement with the same aperture on the models, where an unresolved flux component could be added at the position of the star. Excluding calibration uncertainties, the measured flux density within a 0.5 arcsec radius aperture on the 18-μm image was 48 $\pm$ 4 mJy of flux, with a photospheric contribution of 33 mJy (75 per cent of total photospheric flux, measured in the same aperture using a scaled PSF). The same measurement on the model with no stellar or unresolved flux component added gives 16 mJy. Therefore the maximum unresolved component that can be added to the model that does not exceed a 3σ upper limit of the observations is 12 mJy. However these measurements do not account for the 12 per cent calibration uncertainty in the photometry or the error in photospheric flux due to uncertainties in the spectral fitting to the star, which is ± 1.2 mJy (on total photospheric flux). Since a change in calibration would also result in a corresponding change in the model flux (to fit the peaks at the correct level), it is instructive to consider what would have been derived with a revised calibration factor and stellar flux. In the extreme situation that the calibration was 36 per cent higher (i.e. a 3σ upper limit on the calibration factor) and the stellar

flux was lower by 3.2 mJy (3σ lower limit), the flux measured in the previously described apertures would have been 65 ± 5 mJy with a corresponding model flux of 22 mJy. Thus the excess would have been 13 ± 5 mJy and so gives a maximum unresolved component of <28 mJy for a 3σ deviation in both calibration and statistical uncertainty.

4.4 Pericentre glow model

The brightness asymmetry seen in Fig. 1 is reminiscent of that seen in the disc of HR 4796 (Telesco et al. 2000). The 6 per cent asymmetry of HR 4796 was interpreted as a consequence of pericentre glow, where the secular gravitational perturbations of a planet on an eccentric orbit imposes a forced eccentricity on the planetesimal belt, causing the forced pericentre side of the disc to be closer to the star and hence hotter and brighter (Wyatt et al. 1999). Here we applied the same model to the HD 191089 disc. The disc is defined by the inner and outer semimajor axis of the disc, a_{min} and a_{max} with a proper eccentricity $e_p = 0$ (so a_{min} and a_{max} are equivalent to r_{min} and r_{max} in the axisymmetric model), the power-law index for the distribution of semimajor axes $\gamma_{PG} = \gamma + 1$, where γ is the surface density index from the axisymmetric model, and a forced eccentricity e_f. The best-fitting model has parameters $a_{min} = 28$, $a_{max} = 90$, $\gamma_{PG} = 2.5$ and $e_f = 0.12$ and is shown in Fig. 5.

This addition of an extra parameter (the forced eccentricity) improves the $\chi^2_{r_{combined}}$ from 1.31 to 1.15, but in general adding an extra parameter will improve the fit of any model. However, given the tentative (1.8σ) nature of the asymmetry, is adding this extra parameter to the model justified? We assess the justification for this extra parameter through use of the Bayesian Information Criterion (BIC):

$$\text{BIC} = N \ln(\chi^2_{r_{combined}}) + k \ln N,$$

where N is the number of data points, k is the number of free parameters and $\chi^2_{r_{combined}}$ is the minimum combined reduced χ^2 for the model. The BIC considers the fit of the model but penalizes the model for extra parameters (see Wahhaj et al. 2005; Liddle 2007). Two models were considered: the axisymmetric disc model (see Section 4.1) and the pericentre glow model (see Section 4.4). The

BIC value for the axisymmetric disc is 19.3 and for the pericentre glow model is 19.2. There is very little difference between the BIC values, indicating that there is no preference between the two models.

5 DISCUSSION

5.1 Implications for the planetary system

There are three different possible interpretations of the state of planet formation in the HD 191089 system based on the resolved image: (i) the inner cavity and brightness asymmetry are due to the formation of planets interior to the inner edge of the resolved disc (Section 5.1.1), (ii) the disc is in the process of forming Pluto-sized bodies as in the delayed stirring models of Kenyon & Bromley (2005) (Section 5.1.2) or (iii) the disc is a remnant of the protoplanetary disc (Section 5.1.3).

5.1.1 Planet in the central cavity

The 18-μm image of HD 191089 shows a resolved belt of dust from 28 to 90 au, inclined at $35°$ from edge on with a cleared inner region extending to a radius of $\sim$28 au. The brightness asymmetry seen in the HD 191089 disc could be evidence for a planet on an eccentric orbit (see Section 4.4). The pericentre glow model only places constraints on the forced eccentricity imposed on the debris disc by the planet's secular perturbations and this cannot be used to constrain its mass and semimajor axis. The only constraint is that the lower the mass of the planet the longer the secular precession time-scales.

Although it is not known it seems likely that should such a planet exist, the same planet that is causing the asymmetry is causing the inner edge, as proposed by Quillen (2006). The inner edge of the resolved dust belt at 28 au could therefore mark the outer edge of the planetary system, especially if a giant planet is sculpting the inner edge of the disc, as in the case of Fomalhaut (Kalas et al. 2008; Chiang et al. 2009) which has a dust belt with a well-defined inner edge and a brightness asymmetry.
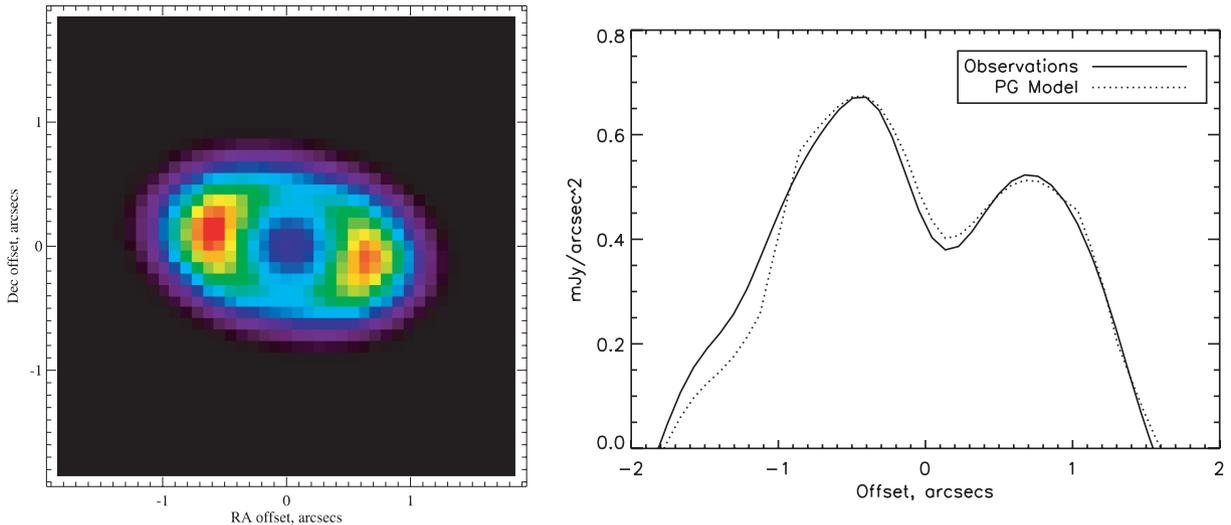

Figure 5. The best-fitting disc from the pericentre glow model which is scaled and shown in the same way as the HD 191089 residuals (Fig. 1) for comparison. The disc parameters are the same as those for the best-fitting axisymmetric disc shown in Fig. 3 (28–90 au, $i = 35°$, $\Sigma \propto r^\gamma$). Right: linecut through the observed and model images at a PA of $80°$ (observed: solid line; model: dotted line).

The steepness of the inner edge of the disc also suggests truncation by a planet. For a disc that extends inward to ~5 au, like the discs seen in Kenyon & Bromley (2004), a surface density of $\Sigma \propto r^6$ from 5 to 8 au is required to satisfy the observed 3σ upper limit of 27 mJy (see Section 4.3) on emission from this region. This is steeper than surface density profile of $\Sigma \propto r^{7/3}$ predicted in the models of Kenyon & Bromley (2004). For a surface density profile like those of the delayed stirring models to be consistent with the observations, then the disc would have to be truncated at 24 au. Assuming the disc is being truncated by a planet at just inside 28 au and that the disc is currently being stirred, then this constraint on the secular time-scale means a minimum mass for the perturber can be derived using equation (42) from Wyatt et al. (1999) which gives a minimum planet mass of $2.6\,M_\oplus$ for a system age of 12 Myr.

5.1.2 Delayed stirring model

Another possible interpretation of these observations is that the resolved belt corresponds to a region of a more extended disc that has recently formed Pluto-sized objects. In these self-stirred models of Kenyon & Bromley (2005) the evolution of an extended planetesimal belt is followed, allowing both the velocity and size distributions to evolve self-consistently. A destructive collisional cascade is only ignited in the disc when planets forming in the disc reach Pluto size. The time-scale for the formation of these Pluto-sized objects depends strongly on their distance from the star and on the surface density of the disc so the outer disc regions are stirred at later times. We performed further modelling based on the prescriptions for the evolution given in Wyatt (2008) and refined in Kennedy & Wyatt (2010) which provides an empirical fit to the self-stirred models of Kenyon & Bromley (2005). This model consists of a planetesimal belt with radii r_{min} and r_{max} with surface density scaled to the MMSN divided into annuli at different radii which have a suppressed dust production rate until the time at which Pluto-sized bodies have formed, stirring the annulus into a destructive collisional cascade, increasing the production of small dust and causing it to brighten. The dust emission is calculated assuming emission from dust grains with a size distribution and composition consistent with the SED and image modelling in previous sections and a ratio of dust area to planetesimal mass appropriate for a collisional cascade size distribution. To account for deviations from this theoretical size distribution a scaling factor η was applied to the surface brightness of the whole disc. However, under these constraints from the SED and with the stirring time set to the age of HD 191089 (12 Myr) the model provided a poor fit to the observations. This is primarily due to the shape of the surface density distribution produced. To produce enough emission in the outer regions of the disc (i.e. out to ~90 au) there has to be a region of gradually rising surface density (with a power law form $\Sigma \propto r^{7/3}$) in the inner region of the disc (see Kennedy & Wyatt 2010, fig. 2). For reasons similar to those discussed in Section 5.1.1 this overproduces emission at <28 au (0.5 arcsec), where the 3σ upper limit on the flux in this region is 27 mJy. Therefore the delayed stirring model cannot fit the sharp inner edge to the disc. However this can be achieved if there is an additional mechanism truncating the disc. For example a disc with an inner radius of 24 au, surface density profile $\Sigma \propto r^{7/3}$ between 24 and 34 au and $\Sigma \propto r^{-1.5}$ from 34 to 90 au can fit the observations. This gives a flux of 26 mJy in the inner 28 au (0.5 arcsec) of the disc, consistent with the 3σ upper limit. We conclude that some mechanism must be truncating the disc, and that it is not possible to determine from these observations

alone whether planet formation is ongoing in some or all of the outer disc.

5.1.3 Protoplanetary disc remnant

A further possibility is that this disc is a remnant of the protoplanetary disc and the dust is confined in a ring due to interactions with gas that remains in the system from the protoplanetary phase (Takeuchi & Artymowicz 2001; Besla & Wu 2007). These models are too gas rich for HD 191089 as a massive gas disc around a star of this age would be unusual as most gas discs are thought to dissipate in <10 Myr (e.g. Hollenbach et al. 2005). Gas has been detected around four A stars known to have debris discs (β Pic: Brandeker et al. 2004; 49 Ceti: Dent, Greaves & Coulson 2005; HD 141569: Jonkheid et al. 2006; HD 32297: Redfield 2007) and its effect on dust is debated; Krivov et al. (2009) concluded that gas does not affect the dust distribution in β Pic, though Besla & Wu (2007) discussed how gas may be undetected and still have an effect on the dust dynamics. Deep gas observations towards HD 191089 would be needed to rule out this effect.

5.2 Placing HD 191089 into context: comparison with F stars of the BPMG

The BPMG is a collection of young (~12 Myr) stars with common proper motion, indicating that they formed in the same cluster which is now dispersing. Their velocities can be traced back to this common point of origin. The age of the moving group can be assessed using the M star members, and the group is then assumed to be coeval. Table 2 gives a census of the currently known F star members of the β Pic Moving Group. Membership was taken from Lépine & Simon (2009), who assessed the membership of the moving group by examining stellar proper motions. By studying the fraction of these stars that have infrared (IR) excesses we can place HD 191089 into context with its coeval moving group. Of the nine known F star BPMG members, six have IR excesses, three of which have resolved debris discs: HD 15115 (Kalas, Fitzgerald & Graham 2007), HD 181327 (Schneider et al. 2006; Chen, Fitzgerald & Smith 2008) and HD 191089 (this work).

For the six stars with discs SED fitting was used to estimate radius and fractional luminosity, which are given in Table 2, and range from 10 to 150 au, and from 3×10^{-5} to 3×10^{-3}. HD 191089 is the second brightest and has the second smallest inner radius. It is the most similar to HD 181327 which is slightly brighter and larger. The similarity is also apparent in images. HD 181327 has been imaged in both scattered light using *Hubble Space Telescope* (*HST*; Schneider et al. 2006) and in mid-IR thermal emission (Chen et al. 2008). This disc shows an extended icy 'Kuiper belt' at 86 au with a width of 36 au (Schneider et al. 2006), compared to a belt at 55 au with a width of 50 au for HD 191089. Both these discs have cleared inner regions (HD 181327 ~68 au, HD 191089 ~28 au) and both show evidence for a brightness asymmetry between the two sides of the disc in the mid-IR (HD 181327: flux ratio of 1.4 ± 0.1 between the northern and southern arms HD 191089: flux ratio of 0.8 ± 0.12 between the east and west sides of the disc).

The other resolved disc HD 15115 is a very large, highly asymmetric disc, dubbed the 'blue needle' due to the elongation of the west side of the disc to >550 au (east side ~310 au) (Kalas et al. 2007). Such an extreme asymmetry could be due to a stellar fly-by, and HIP 12545 (also a member of the BPMG) is a possible candidate due to its near on-sky position (Kalas et al. 2007). This

Table 2. Census of F star members of the BPMG. The dust radius is calculated by fitting a blackbody to the 24 and 70 μm fluxes, or from previous literature blackbody fits to the SED.

Star	Spectral type	Mass ($M_\odot$)	Distance (pc)	Luminosity ($L_\odot$)	$\frac{L_{Dust}}{L_*}$	Blackbody dust radius [resolved] (au)	Refs	Notes
HD 203	F3V	1.3	39.1	2.7	1×10^{-4}	10	1, 2,3,4	1
HD 14082A	F5V	1.23	39.42	1.88	N/A	N/A	1,2,3,4	2 (binary)
HD 15115	F2V	1.39	44.8	2.94	4.9×10^{-4}	34 [~300–500]	5,6,7	3 (resolved disc)
HD 29391	F0V	1.27	29.9	5.85	N/A	N/A	1	4 (binary)
HD 35850	F7V	1.19	26.8	1.78	3×10^{-5}	150	1,8,9,10,11	5
HD 164249	F5V	1.32	46.8	2.64	5.9×10^{-4}	20	1	6
HD 181327	F5/6V	1.3	51	3.1	3×10^{-3}	20 [86]	7,1,6,12,13	7 (resolved disc)
HD 191089	F5V	1.4	54	3.2	1.4×10^{-3}	15 [55]	1,7,8,14	
HD 199143	F8V	1.2	48	2.45	?	?	15,16,17,18	8

References: 1 – Rebull et al. (2008); 2 – Carpenter et al. (2008); 3 – Lépine & Simon (2009); 4 – Carpenter et al. (2009); 5 – Kalas et al. (2007); 6 – Moór et al. (2006); 7 – Chen et al. (2006); 8 – Roccatagliata et al. (2009); 9 – Perryman et al. (1997); 10 – Spangler et al. (2001); 11 – Silverstone et al. (2006); 12 – Chen et al. (2008); 13 – Moshir et al. (1993); 14 – Chen et al. (2006); 15 – Jayawardhana & Brandeker (2001); 16 – Kaisler et al. (2004); 17 – van den Ancker et al. (2000); 18 – Chauvin et al. (2002).

Notes. 1 – strong *Spitzer* 24 μm excess ($F_{24} = 60F_{*24}$; Carpenter et al. 2009); 2 – binary companion HD 14082B (G5V, 530 au separation; Song et al. 2003); 3 – resolved asymmetric debris disc 'blue needle'. Possibly perturbed by HIP 12545 flyby (Kalas et al. 2007); 4 – binary companion (~800 au). Blended with *Spitzer*; 5 – dust based on *Spitzer* 70 μm excess (Silverstone et al. 2006); 6 – dust based on *Spitzer* 24 and 70 μm excess (Rebull et al. 2008); 7 – resolved disc at ~86 au (~20 au width; Schneider et al. 2006; Chen et al. 2008); 8 – binary companion (M2, 86 au; Kaisler et al. 2004). Possible circumsecondary disc (van den Ancker et al. 2000; Chauvin et al. 2002; Kaisler et al. 2004).

asymmetry could also be caused by interaction with a nearby interstellar medium (ISM) cloud, that could be 'sandblasting' and so stripping material from one side of the disc (Debes, Weinberger & Kuchner 2009; Maness et al. 2009). There are not many obvious similarities between HD 191089 and HD 15115: the unusual morphology of HD 15115 appears to originate through interaction with an external perturber rather than due to any planets in the system and it appears much more extended in images than HD 191089. Vega's disc displays a similarly extended shape to HD 15115, with a high population of small grains in the process of being blown out of the system (Su et al. 2005). However, this system can still be explained in the context of a steady state collisional cascade when the difference in stellar luminosity between the pole and equator due to Vega's fast rotation is taken into account (Müller, Löhne & Krivov 2010).

The remaining three stars are all binaries, and one of these, HD 199143, may show some evidence for a IR excess due to a circumsecondary disc (Jayawardhana & Brandeker 2001), but this may simply be due to uncertainties in the photospheric modelling of the binary companion (van den Ancker et al. 2000; Chauvin et al. 2002; Kaisler et al. 2004). The general lack of excess seen for the F stars of the BPMG that are also binaries could be due to perturbations from the secondary truncating any possible discs. HD 199143 has a separation of ~53–105 au (Jayawardhana & Brandeker 2001; Chauvin et al. 2002) and there is observational evidence that binary companions in the range 50–100 au are expected to disrupt discs (Jensen, Mathieu & Fuller 1994). The other two binaries have quite wide predicted separations (HD 14082: ~530 au, Song, Zuckerman & Bessell 2003; HD 29391: ~800 au, Feigelson et al. 2006), and unless on very eccentric orbits the secondaries are unlikely to preclude the presence of discs around the primaries in these systems. It is possible that the binary has evolved or that there is something about the formation mechanism of binary systems that suppresses formation or detectability of a debris disc, but the small number statistics for this sample means that this is still inconclusive.

6 CONCLUSIONS

We have presented *Qa*-band Gemini T-ReCs imaging of the 12 Myr old F star HD 191089. The emission at 18.3 μm is shown to be significantly extended compared with a point source. This image represents the first resolution of dust emission around this star. These observations confirm the interpretation of the SED as a debris disc with a single component resolved at 28–90 au. There is little emission from the inner 28 au of the disc, indicating the presence of an inner cavity.

The disc also shows a tentative brightness asymmetry of $F_W/F_E = 0.80 \pm 0.12$ with a significance of 1.8σ. This asymmetry is consistent with a scenario in which an perturbing body on an eccentric orbit imposes a forced eccentricity of 0.12 on the planetesimal belt through secular perturbations, causing the centre of the ring to become offset from the star which replicates the brightness asymmetry observed. This interpretation can be tested by further observations seeking to confirm the brightness asymmetry and measure the predicted offset of the star from the centre of the ring.

To predict the surface brightness of the HD 191089 disc in scattered light we used $S = F\tau\omega/4\pi\phi^2$ (Weinberger et al. 1999), where S is the surface brightness (mJy arcsec^{-2}), F is the stellar flux (mJy), τ is the optical depth, ω is the albedo and ϕ is the angular distance of the disc from the star. Using our best-fitting model parameters at Near Infrared Camera and Multi-Object Spectrometer (NICMOS) wavelengths ($\lambda_c = 1.1, \Delta\lambda = 0.59$) we predict a surface brightness of 0.024–0.19 mJy arcsec^{-2} assuming isotropic scattering and an albedo of 0.1–0.8 the range predicted for Kuiper belt objects (Stansberry et al. 2008). Although this is detectable with Advanced Camera for Surveys (ACS) and NICMOS resolving the disc would be difficult as the peak surface brightness is expected at a radius of 1 arcsec, which will be close to the inner working edge of the coronograph for NICMOS observations, and inside it for ACS.

Three models for the central hole were considered. The interpretation that fits most neatly with the model for the brightness

asymmetry is that the inner region has been cleared of planetisimals by a planetary system. In this case high-resolution images of the system could resemble Fomalhaut, including a planet close to the inner edge of the belt. We found that the sharpness of the inner edge was incompatible with the delayed stirring models (Kenyon & Bromley 2004) in which the disc is in the process of forming Pluto-sized objects causing the disc to brighten at the radii where they have just formed, although it is possible that planet formation of the type envisioned by these models is ongoing as long as some other process is truncating the disc at 25 au. A third possibility is that the planetesimal belt is somehow confined due to dynamical interactions with gas in the system. However, there are no observational constraints on the presence of gas in the HD 191089 system. When compared to other members of the BPMG, the most obvious similarities in terms of fractional luminosity and radius inferred from blackbody fitting are with HD 181327, which has also been resolved at mid-IR wavelengths (Chen et al. 2008) and shows evidence for an inner clearing and asymmetry similar to those seen in HD 191089.

REFERENCES

Adelman S. J., 2001, A&A, 367, 297
Andrews S. M., Williams J. P., 2005, ApJ, 631, 1134
Augereau J. C., Lagrange A. M., Mouillet D., Papaloizou J. C. B., Grorod P. A., 1999, A&A, 348, 557
Backman D. E., Paresce F., 1993, in Levy E. H., Lunine J. I., eds, Protostars and Planets III. Univ. Arizona Press, Tucson, p. 1253
Bernstein G. M., Trilling D. E., Allen R. L., Brown M. E., Holman M., Malhotra R., 2004, AJ, 128, 1364
Besla G., Wu Y., 2007, ApJ, 655, 528
Bohren C. F., Huffman D. R., 1983, Absorption and Scattering of Light by Small Particles. Wiley, New York
Brandeker A., Liseau R., Olofsson G., Fridlund M., 2004, A&A, 413, 681
Burns J. A., Lamy P. L., Soter S., 1979, Icarus, 40, 1
Carpenter J. M. et al., 2008, ApJS, 179, 423
Carpenter J. M. et al., 2009, ApJS, 181, 197
Chauvin G. et al., 2002, A&A, 394, 219
Chen C. H. et al., 2006, ApJS, 166, 351
Chen C. H., Fitzgerald M. P., Smith P. S., 2008, ApJ, 689, 539
Chiang E., Kite E., Kalas P., Graham J. R., Clampin M., 2009, ApJ, 693, 734
Cohen M., Walker R. G., Carter B., Hammersley P., Kidger M., Noguchi K., 1999, AJ, 117, 1864
Currie T., Kenyon S. J., Balog Z., Rieke G., Bragg A., Bromley B., 2008, ApJ, 672, 558
Debes J. H., Weinberger A. J., Kuchner M. J., 2009, ApJ, 702, 318
Dent W. R. F., Greaves J. S., Coulson I. M., 2005, MNRAS, 359, 663
Dohnanyi J. W., 1969, J. Geophys. Res., 74, 2531
Feigelson E. D., Lawson W. A., Stark M., Townsley L., Garmire G. P., 2006, AJ, 131, 1730
Haisch K. E., Jr, Lada E. A., Lada C. J., 2001, ApJ, 553, L153
Hillenbrand L. A. et al., 2008, ApJ, 677, 630
Hollenbach D. et al., 2005, ApJ, 631, 1180
Jayawardhana R., Brandeker A., 2001, ApJ, 561, L111
Jensen E. L. N., Mathieu R. D., Fuller G. A., 1994, ApJ, 429, L29
Jonkheid B., Kamp I., Augereau J., van Dishoeck E. F., 2006, A&A, 453, 163
Kaisler D., Zuckerman B., Song I., Macintosh B. A., Weinberger A. J., Becklin E. E., Konopacky Q. M., Patience J., 2004, A&A, 414, 175
Kalas P., Fitzgerald M. P., Graham J. R., 2007, ApJ, 661, L85
Kalas P. et al., 2008, Sci, 322, 1345
Kennedy G. M., Wyatt M. C., 2010, MNRAS, 405, 1253
Kenyon S. J., Bromley B. C., 2004, ApJ, 602, L133
Kenyon S., Bromley B., 2005, AJ, 130, 269
Krivov A. V., Herrmann F., Brandeker A., Thébault P., 2009, A&A, 507, 1503
Kurucz R. L., 1979, ApJS, 40, 1
Lagrange A. et al., 2009, A&A, 493, L21
Lépine S., Simon M., 2009, AJ, 137, 3632
Li A., Greenberg J. M., 1997, A&A, 323, 566
Liddle A. R., 2007, MNRAS, 377, L74
Luhman K. L., Allen P. R., Espaillat C., Hartmann L., Calvet N., 2010, ApJS, 186, 111
Maness H. L. et al., 2009, ApJ, 707, 1098
Mannings V., Barlow M. J., 1998, ApJ, 497, 330
Moór A., Ábrahám P., Derekas A., Kiss C., Kiss L. L., Apai D., Grady C., Henning T., 2006, ApJ, 644, 525
Moshir M. et al., 1993, VizieR Online Data Catalog, 2156, 0
Müller S., Löhne T., Krivov A. V., 2010, ApJ, 708, 1728
Muzerolle J., Allen L. E., Megeath S. T., Hernández J., Gutermuth R. A., 2010, ApJ, 708, 1107
Nordström B. et al., 2004, A&A, 418, 989
Perryman M. A. C., Lindegren L., Kovalevsky J., 1997, A&A, 323, L49
Quillen A. C., 2006, MNRAS, 372, L14
Rebull L. M. et al., 2008, ApJ, 681, 1484
Redfield S., 2007, ApJ, 656, L97
Roccatagliata V., Henning T., Wolf S., Rodmann J., Corder S., Carpenter J. M., Meyer M. R., Dowell D., 2009, A&A, 497, 409
Schneider G. et al., 2006, ApJ, 650, 414
Silverstone M. D. et al., 2006, ApJ, 639, 1138
Smith R., Wyatt M. C., 2010, A&A, 515, 95
Smith R., Wyatt M. C., Dent W. R. F., 2008, A&A, 485, 897
Smith R., Churcher L. J., Wyatt M. C., Moerchen M. M., Telesco C. M., 2009, A&A, 493, 299
Song I., Zuckerman B., Bessell M. S., 2003, ApJ, 599, 342
Spangler C., Sargent A. I., Silverstone M. D., Becklin E. E., Zuckerman B., 2001, ApJ, 555, 932
Stansberry J., Grundy W., Brown M., Cruikshank D., Spencer J., Trilling D., Margot J., 2008, Physical Properties of Kuiper Belt and Centaur Objects: Constraints from the Spitzer Space Telescope. Univ. Arizona Press, Tucson, p. 161
Su K. Y. L. et al., 2005, ApJ, 628, 487
Takeuchi T., Artymowicz P., 2001, ApJ, 557, 990
Telesco C. M. et al., 2000, ApJ, 530, 329
van den Ancker M. E., Pérez M. R., de Winter D., McCollum B., 2000, A&A, 363, L25
Wahhaj Z., Koerner D. W., Backman D. E., Werner M. W., Serabyn E., Ressler M. E., Lis D. C., 2005, ApJ, 618, 385

Weinberger A. J., Becklin E. E., Schneider G., Smith B. A., Lowrance P. J., Silverstone M. D., Zuckerman B., Terrile R. J., 1999, ApJ, 525, L53

Wyatt M. C., 2006, ApJ, 639, 1153

Wyatt M. C., 2008, ARA&A, 46, 339

Wyatt M. C., Dermott S. F., Telesco C. M., Fisher R. S., Grogan K., Holmes E. K., Piña R. K., 1999, ApJ, 527, 918

Wyatt M. C., Greaves J. S., Dent W. R. F., Coulson I. M., 2005, ApJ, 620, 492

Zuckerman B., Song I., 2004, ARA&A, 42, 685

This paper has been typeset from a TEX/LATEX file prepared by the author.